RESEARCH ARTICLE | NOVEMBER 05 2024

Significance of the smaller scales for hypersonic turbulent boundary layers with focused laser differential interferometry

Special Collection: Measurement, Modelling and Prediction of Hypersonic Turbulence

E. K. Benitez; M. Aultman; L. Duan; G. P. Camillo; J. S. Jewell

Physics of Fluids 36, 115123 (2024)
https://doi.org/10.1063/5.0235247

Physics of Fluids ARTICLE pubs.aip.org/aip/pof

Significance of the smaller scales for hypersonic turbulent boundary layers with focused laser differential interferometry

Cite as: Phys. Fluids 36, 115123 (2024); doi: 10.1063/5.0235247
Submitted: 26 August 2024 · Accepted: 14 October 2024 ·
Published Online: 5 November 2024

View Online Export Citation CrossMark

E. K. Benitez,[1,a)] M. Aultman,[2] L. Duan,[2] G. P. Camillo,[3] and J. S. Jewell[4]

AFFILIATIONS

[1]High Speed Systems Division, Air Force Research Laboratory, WPAFB, Ohio 45433, USA
[2]Department of Mechanical and Aerospace Engineering, The Ohio State University, Columbus, Ohio 43218, USA
[3]German Aerospace Center (DLR), Institute of Aerodynamics and Flow Technology, 37073 Göttingen, Germany
[4]School of Aeronautics and Astronautics, Purdue University, West Lafayette, Indiana 47907, USA

Note: This paper is part of the Special Topic, Measurement, Modelling and Prediction of Hypersonic Turbulence.
[a)]**Author to whom correspondence should be addressed:** elizabeth.benitez.2@us.af.mil

ABSTRACT

While designed to suppress disturbances located away from its beam foci, focused laser differential interferometry (FLDI) is known to have some integration of signals along its optical axis. This is especially true for longer-wavelength signals, although smaller-scale flow structures also have a non-infinitesimal sensitivity length. This study investigates the performance of FLDI in a hypersonic turbulent boundary layer to better understand its behavior. FLDI simulations were conducted using both full-scale direct numerical simulation (DNS) and spatially averaged DNS inputs to directly assess the influence of smaller flow structures on FLDI measurements. The full-scale FLDI results indicate that integration along the optical axis likely results in lower FLDI amplitudes than for true point measurements. Comparison with the spatially averaged FLDI simulations reveals the significance of small-scale structures in FLDI signal roll-off and root mean square amplitudes. Further, the influence of FLDI setup parameters on the response across the frequency spectrum are analyzed. Circular, Gaussian beams with smaller widths are verified to present increased performance relative to elliptical or uniform-intensity beams. Also, measurements using distinct differentiation directions suggest an experimental way to measure turbulence isotropy scales. These results have notable implications for understanding hypersonic turbulent boundary-layer dynamics and interpreting experimental data. Distribution Statement A: Approved for Public Release; Distribution is Unlimited. PA# AFRL-2024-4678; Cleared 08/23/2024.

Published by AIP Publishing. https://doi.org/10.1063/5.0235247

I. INTRODUCTION

As hypersonic flight becomes a priority across several nations, understanding the behavior of turbulence at these speeds becomes more important. However, investigating hypersonic turbulence poses a significant challenge due to the extensive range of flow structure sizes that are present simultaneously. In experimental studies of this regime, focused laser differential interferometry (FLDI) has emerged as a prevalent diagnostic tool. FLDI allows for highly sensitive density gradient measurements to be taken at high bandwidths without a physical probe interfering with the flow. It is an ideal choice for making hypersonic aerodynamic measurements, as its focusing ability helps suppress signals away from the region of interest, although the extent of this suppression depends on characteristics of the flowfield being probed. FLDI has, therefore, been studied in multiple computational investigations aimed at comprehending both its effectiveness and constraints, but there is still work to be done to be able to fully interpret measurements from this technique.

FLDI is an optical diagnostic commonly used to measure high-speed fluctuations such as those found in hypersonic boundary-layer instabilities. It was originally created by Smeets and George in the 1970s as a variant of laser differential interferometry specifically designed to diminish the effect of signals away from the point of interest.[1] The technique has been utilized to study turbulent jets,[2–5] shocks,[6–8] freestream disturbances,[9–11] and hypersonic boundary layers.[12–18] It has been modified in a number of ways to expand its usability[4,19–22] and several studies have been conducted to characterize its performance.[18,23–28] Research comparing experimental and simulated FLDI has broadly resulted in good agreement,[3,16,26] although accurate conversion from beam phase change to density fluctuations remains an active problem.[24,27,28]

Prior work has shown that the changing diameter of the beam profiles due to the focusing field lenses is generally the source of the signal rejection measured away from the foci, as opposed to the overlapping spatial positions of the beams. It has also been demonstrated that smaller-wavelength signals experience a shorter sensitivity length along the beams compared to longer-wavelength ones.[23,26] These details introduce a dependence between the beam profiles along the optical path and the wavelengths of the signal to be measured. Hypersonic turbulence is a difficult signal to study due to the broad range of wavelengths involved. A common computational technique for turbulence, large-eddy simulation (LES), neglects small-scale flow structures. LES has been used for FLDI simulations with some agreement, although some differences between computational and experimental FLDI results remain for these cases.[16,26] By utilizing a computational model of FLDI with both a high-resolution and a spatially averaged direct numerical simulation (DNS) of a hypersonic turbulent boundary layer, it is possible to gain understanding in the effect of the smallest-scale structures on an FLDI measurement.

There are two primary objectives for this paper. First, to directly simulate FLDI measurements for a full-scale DNS to understand the behavior of an FLDI when measuring a hypersonic turbulent boundary layer. Second, using the original DNS and a spatially averaged version of it, to study how FLDI is influenced by the small-scale structures in hypersonic turbulent flow. Two FLDI models (one from AFRL and one from DLR) were run with the same DNS inputs to allow for the comparison between code and increase the confidence in the results.

II. COMPUTATIONAL METHODS

Two computational methods are utilized in this study to help understand the significance of the different scales of turbulence with regard to an axisymmetric hypersonic boundary layer. The initial flow field was computed via high-fidelity DNS with conditions selected to match an experiment. Then, the resulting flow field from the high-resolution DNS and a spatially averaged version of it were run through a FLDI simulation to determine how well experimental measurements made with an FLDI replicate the actual fluctuations present in the flow. This simulation was run with the outputs of both the original and spatially averaged DNS to study the importance of the smaller-scale, higher-frequency fluctuations in the final measurements made with that technique.

A. Flow field conditions

The flow field used in the study was computed based on a Mach-8 experiment from the Sandia HWT-8.[29] The test article was a sharp, 7° half-angle cone that was 0.517-m long. The nosetip had a radius of 0.05 mm. The DNS domain extended the cone to be 0.86-m long and was divided into three, overlapping boxes as shown in Fig. 1. Experiments confirmed that the boundary layer state at axial positions greater than 0.3 m was fully turbulent for a freestream unit Reynolds number of 12.8×10^6/m.[29] The model wall temperature was set at 298 K, matching the experimental wall-to-recovery temperature $T_w/T_r \approx 0.54$.[30]

B. Direct numerical simulation (DNS)

The DNS results are described in detail in Huang *et al.*,[30] but are summarized here for reference. Numerical solutions were obtained for

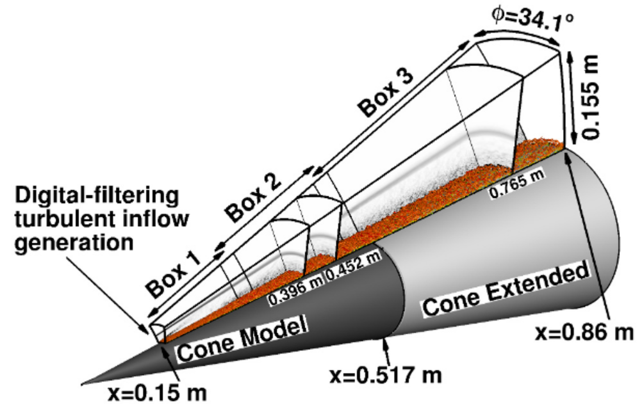

FIG. 1. Flow field of Mach-8 cone. Reproduced with permission from Huang *et al.*, AIAA J. 62, 3 (2024). Copyright 2023 by the American Institute of Aeronautics and Astronautics, Inc.[30]

the complete three-dimensional compressible Navier–Stokes equations in cylindrical coordinates to replicate the turbulent boundary layer on a circular cone. Nitrogen served as the working fluid and operated within the perfect gas regime. The flow was assumed to be Newtonian, with the viscous stress tensor correlating linearly with the rate-of-strain tensor, and Fourier's law establishing a linear relationship between the heat flux vector and the temperature gradient. The coefficient of viscosity (μ) was determined using Keyes law, while the coefficient of thermal conductivity (κ) was calculated as $\kappa = \mu C_p/Pr$. A molecular Prandtl number (Pr) of 0.71 was used. Inviscid fluxes of the governing equations were computed using a seventh-order weighted essentially non-oscillatory (WENO) method.[31] Viscous fluxes were discretized using a fourth-order central difference approach, and time integration was executed with a third-order low-storage Runge–Kutta scheme.[32]

To study the effect of small structures in the flow, a spatially averaged version of the full-scale DNS was also computed. The averaging was achieved by applying a tophat filter with a filter width of $8dx$ or $8dy$ along the streamwise-spanwise plane.[33] The resulting flowfield can be plotted on the same grid with the same temporal resolution, but has the smallest-scale structures of the flow smeared out. Figure 2 shows a planar slice of the original full-scale DNS (DNS_{FS}, where FS is for" full-scale") as well as the spatially averaged version (DNS_{SA}, where SA is for "spatially averaged"). Both fields look very similar, with the primary difference being the resolution of the fluid structures present. In the spatially averaged DNS, small-scale structures are averaged out, essentially creating a flow field that is the same as the original but with larger average structure sizes.

C. Focused laser differential interferometer (FLDI) simulation

The models of FLDI used in this study simulate the region of the beams that pass through the computed density field. Therefore, the optics about this region are not simulated.

1. AFRL FLDI model

FLDI is a technique that estimates density changes in a flow along a single axis by utilizing two closely spaced beams focused at a specific

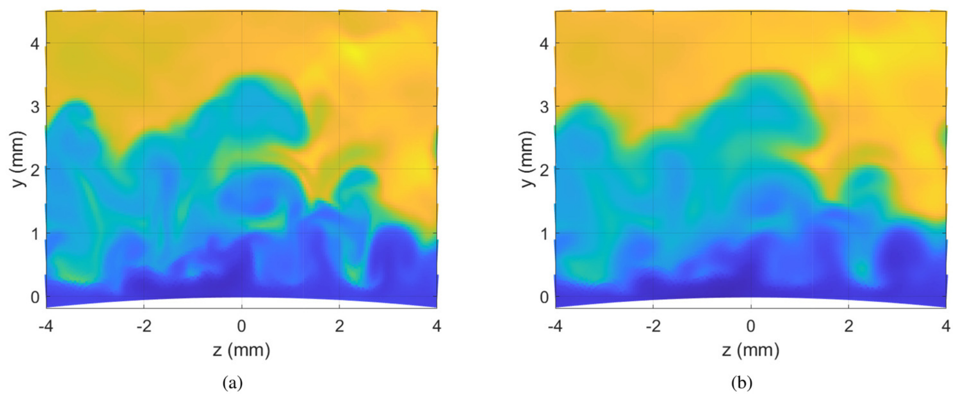

FIG. 2. Subsets of the DNS density fields: (a) original full-scale DNS density field (DNS_{FS}) and (b) spatially averaged DNS density field (DNS_{SA}).

point of interest. This approach employs common-path interferometry since both beams travel through the test gas mostly along the same optical path. In its simplest configuration, as shown in Fig. 3, the FLDI setup involves just a laser, a photodiode (or camera) to make the measurement, three lenses, and two polarizers and prisms. The coherent light emitted by the laser is polarized using polarizing element P1, and then, expanded through a concave lens (L1). A small-angle birefringent prism (Pr1) splits the beam into two orthogonally polarized beams, which are subsequently focused and parallelized by a convex lens (L2) at a separation distance of Δx. The focal points of the FLDI are the most sensitive regions, where the two beams have the smallest diameters and do not overlap in space. To maintain symmetry, the setup includes another lens (L3) that refocuses the beams on the opposite side of the foci. The beams then pass through another birefringent prism (Pr2) with the same splitting angle to collocate the light. At this stage, the beams do not interfere since they remain orthogonally polarized. The light is further transmitted through a polarizer (P2) to enable interference. Finally, the intensity of the resulting beam is measured using a photodiode or camera.

FLDI is capable of making quantitative measurements by leveraging the linear correlation between the density of a fluid and its refractive index, which is characterized by the Gladstone–Dale constant.[34] As each beam travels through a slightly distinct local density field, a relative phase shift is generated between them. Consequently, the interference of the initial beams induces variations in the intensity of the resulting beam, enabling direct measurement of this phase shift.

The computational FLDI model used in this study was originally developed by Schmidt and Shepherd,[23] and utilizes a ray-tracing methodology to estimate the FLDI signal at the photodiode. It was successfully used to study FLDI responses to various flow phenomena, generally in the hypersonic regime.[7,10,16,25,26] A complete derivation for the current implementation can be found in Benitez *et al.*[26] The resulting equation for the total phase shift due to a given density field is described by the following equation:

$$\Delta\Phi = \frac{2K\pi}{\lambda}\int\int_P I_0(\alpha,\beta)\left(\int_{s_1}\rho(\mathbf{x_1})ds - \int_{s_2}\rho(\mathbf{x_2})ds\right)d\alpha d\beta. \quad (1)$$

Here, K is the Gladstone–Dale constant, λ is the wavelength of the laser, I_0 is the local intensity of the beam at location (α, β) in the beam profile plane, and ρ is the local density. P represents the beam profile plane, while $\mathbf{x_i}$ is the three-dimensional location of the local density for beam i and s_i is the beam path for beam i. Since the optical paths of the two beams largely overlap, $s_1 = s_2 = s$, so Eq. (1) can be simplified further:

$$\Delta\Phi = \frac{2K\pi}{\lambda}\int_s\left[\int\int_P(\rho(\mathbf{x_1}) - \rho(\mathbf{x_2}))I_0(\alpha,\beta)d\alpha d\beta\right]ds. \quad (2)$$

This equation can be solved computationally for a given density field. For a time-varying case, it can be looped for each point in time, to get a time series $\Delta\Phi(t)$.

The FLDI beams were discretized across both the profile plane and the optical axis. For these simulations, the optical (z) axis was divided evenly into 5150 points between $z = \pm 50$ mm. Each beam profile was defined by 65 341 grid points split uniformly in angle and clustered around the centroid in radius, and each beam has 10 299 profile planes defined along the z-axis. Figure 4 displays the normalized grid used for each beam profile plane, with 363 points in the radial direction and 180 points azimuthally. With two FLDI beams, the total number of potential grid points is 1 345 893 918; however, only z locations defined within the DNS flowfield are actually computed. For this case, that limited the optical axis to between ± 16 mm, resulting in 431 119 918 grid points actually simulated.

There are several methods to convert from the beam phase change $\Delta\Phi(t)$, which represents a spatial gradient, to the local flow

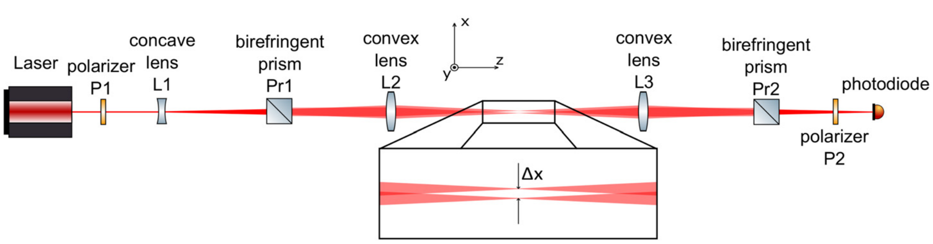

FIG. 3. An illustration of a simple FLDI.

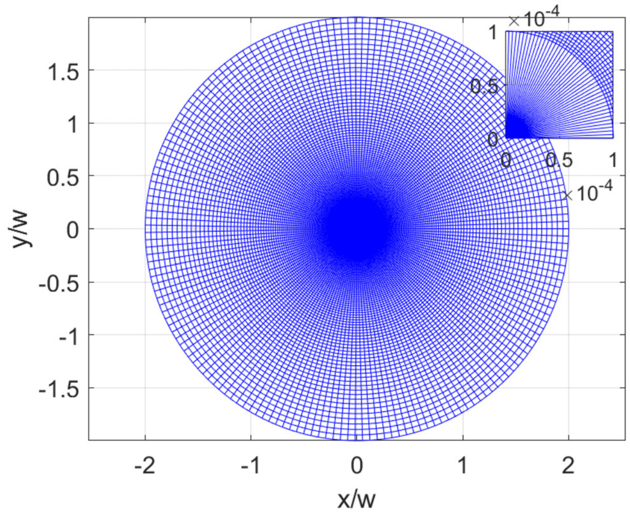

FIG. 4. Grid used to discretize beam profile.[26]

density fluctuations $\rho'(t)$, which is a temporal fluctuation.[5,23,25,27,35,36] However, these all require some assumptions about either the sensitivity distribution of the FLDI or the behavior of the flow field. For this work, the results are left as a density difference, $\Delta\rho$, to avoid some of these assumptions. However, to convert from $\Delta\Phi$ to $\Delta\rho$, a sensitivity length L was computed using the estimation method described by Lawson and Austin,[28] where L is a function of the frequency, f. This function is displayed in the following equation:

$$L(f) = \frac{2\sqrt{2}w_0}{\lambda} \cdot \frac{u_c}{f} \cdot erf^{-1}(0.99). \tag{3}$$

Here, we define u_c as 80% of the freestream velocity ($u_c = 0.8u_\infty = 860$ m/s).[30]

The $\Delta\Phi$ data were then converted to $\Delta\rho$ using Eq. (4). Note that both $\Delta\Phi$ and $\Delta\rho$ are functions of time, t, rather than frequency, f:

$$\Delta\rho(t) = \Re\left[\mathscr{F}^{-1}\left\{\frac{\lambda}{2\pi K L(f)} \circledast \mathscr{F}\{\Delta\Phi(t)\}\right\}\right]. \tag{4}$$

For this process, $\mathscr{F}$ represents the fast Fourier transform executed in MATLAB (`fft`), while $\mathscr{F}^{-1}$ is the inverse fast Fourier transform (`ifft`). The circular convolution, $\circledast$ (`cconv` in MATLAB), is utilized since the scaling occurs in frequency space, which differs from the usual multiplication in temporal space. The real component of the solution, $\Re$, is taken after finding the inverse Fourier transform.

The original flow field density values for each time step, $\rho(\mathbf{x}, t)$, are from the DNS described previously. Due to the large size of the DNS, the flow field was divided into five separate regions in the vertical direction, with each region having the same number of data points, before running through the FLDI simulation. The DNS flow fields were rotated so that the model wall was tangent to the $x - z$ plane, and the density data were read as scattered data in MATLAB. In this paper, simulated FLDI density differences are compared to DNS-derived density differences, which were found by taking the DNS densities at the center of each foci and subtracting them.

The coordinate system used for the FLDI simulation has its origin on the surface of the cone, located axially between the two foci. The beams are split in the streamwise direction, such that one is directly upstream of the other and they are both the same normal height from the model surface. The x axis is in the direction of the flow, while the y axis is normal to the surface. The z axis is along the laser path.

In addition to the overall simulated FLDI measurements, planar FLDI measurements were also saved at each optical-axis position. These deconstructed measurements allow for studying the combined effect of the FLDI averaging across each beam profile and the overlap of the two beams for each spanwise station, without the effect of the overall integration along the optical axis. Due to the exclusion of the optical-axis integration, converting from these planar beam phase change values to density difference does not involve computing an integration length. Instead, the planar density change is directly calculated using the following equation:

$$\Delta\rho(t) = \frac{\lambda}{2\pi K}\Delta\Phi(t). \tag{5}$$

Simulated FLDI parameters were selected to be similar to FLDI configurations that have previously been used in experiments.[4,26] Three Gaussian beam profiles were used for the simulation with the beam profiles defined by the following equation:

$$w(z) = w_0\sqrt{1 + \left(\frac{\lambda z}{\pi w_0^2}\right)^2}. \tag{6}$$

The beam waists (w_0) of 3, 5, and 7 μm were selected to test (Fig. 5). A laser wavelength of 633 nm was utilized with a separation of 150 μm between the two beams. Simulated FLDI measurements were taken 0.396 m downstream of the sharp nosetip, with the beams split parallel to the model surface.

2. DLR FLDI model

In addition to the AFRL computational FLDI model, the FLDI code in operation at the DLR-Göttingen was also used in this work. A

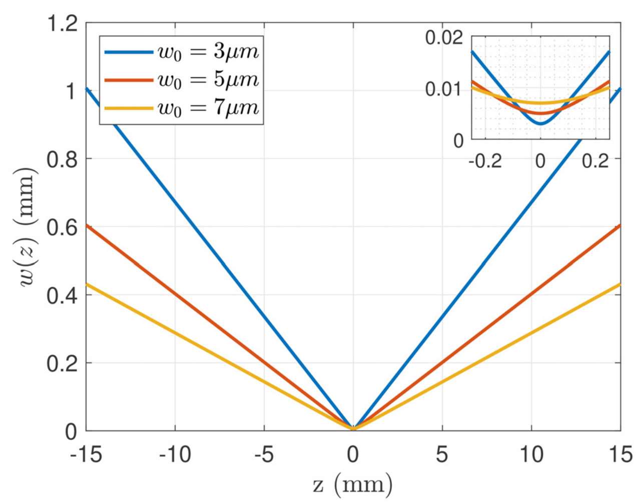

FIG. 5. Beam waist from Gaussian beam profiles used for the FLDI analysis.

detailed description of the DLR FLDI model, as well as a validation case, can be found in Camillo and Wagner.[8]

The DLR model is also based in the original development of Schmidt and Shepherd,[23] such that the basic equations are identical to the ones in the AFRL model described in the previous section. However, the two models have been independently implemented, presenting important differences which are clarified below.

For Eq. (2) to be evaluated, the density values at each FLDI grid point must be interpolated from the original flow field mesh. As explained in Sec. II C 1, the AFRL model approaches the density field as scattered data to perform this evaluation, but requires the field to be rotated and translated so that the FLDI beams are located in the desired position. Using scattered data has the advantage of universal applicability, regardless of the form of the computational flow field, but requires some preprocessing of the flow field to ensure the input data are not too large for the computation.

The DLR model, conversely, uses a coordinate transformation to represent the density values on a three-dimensional rectangular grid. In this rectangular coordinate system, the grid variables each vary along a single dimension of the grid. The FLDI grid points are then transformed accordingly onto the same coordinate system before performing the interpolation. For this model, the flow field requires preprocessing to structure the flow field grid, but the FLDI grid is later positioned within it. The approach adopted in the DLR model is only applicable to computational flow fields with well-defined laws for mesh definition, such as Cartesian, conical, or some types of more complex structured meshes. However, with the density values represented in a rectangular grid, computationally light interpolation tools such as MATLAB's `interpn` may be used to evaluate the FLDI grid points. As a result, the calculation of the FLDI response on each time step of the flow field can be less computationally intensive. Therefore, the flow field did not need to be split into separated components for the numerical analysis with this code.

Taking advantage of the capability of the DLR model to sweep over different parameters inexpensively, it is used in the present work as a parametric analysis tool. The effects of different characteristics of the FLDI instrument in comparison to a standard case are analyzed in the context of hypersonic turbulent boundary layer investigation. This analysis will be shown in Sec. III B, together with a direct comparison between the AFRL and DLR model outputs.

The discretization of the FLDI beams for the DLR model was defined following a grid convergence analysis, facilitated through the use of rectangular grids. Same as the AFRL model, the grid points are clustered around the centroid of each beam. The azimuthal direction was divided in 36 points, with the radial direction having 45 points distributed such that the aspect ratio of each grid cell was close to 1. Along the optical axis, between 700 and 770 planes were used, depending on the off-surface location. The total number of grid points for each FLDI beam was hence approximately 1 200 000. This grid discretization was verified to produce results equivalent to a finer mesh with approximately 20 000 000 points.

III. RESULTS

A. AFRL FLDI simulation results

Two versions of the DNS flow field were utilized to simulate FLDI measurements of the hypersonic turbulent boundary layer. The original, full-scale DNS and a spatially averaged variant were run through the FLDI simulation with three different Gaussian-beam waists to see how each beam set would respond to the same density field with and without small-scale flow structures.

1. Full-scale DNS

To understand how the FLDI processes the more realistic flow field, simulated FLDI measurements through the full-scale DNS were made at different off-surface heights for each of the three beam waist sizes (3, 5, and 7 μm). The FLDI signal was processed as described in Sec. II C to convert the computed beam phase change values to density difference. To compare the FLDI results to the "true" values from the DNS, the density difference between the foci centers was extracted from the DNS for each time step and off-surface height.

Figure 6 gives an overview of the simulated FLDI results as compared to DNS density differences for the 5 μm beam waist. Figures 6(a) and 6(b) show the time series for both the DNS-derived and FLDI-simulated cases, while Figs. 6(c) and 6(d) display the power spectral densities (PSDs) for each. Note that the color scale for the DNS and FLDI results are different; this is most likely due to the integration along the optical axis from the FLDI, and will be discussed later. Qualitatively, the time series between the DNS and FLDI are similar, with the FLDI appearing more smeared and overall having a lower amplitude. For the PSDs, the FLDI again has lower amplitudes than the DNS, and also appears to suppress more of the lower frequencies. This lower-frequency suppression is due to the finite spacing between the beams, and will be discussed in Sec. III A 3.

To get a better understanding of the scales involved in this flowfield, Fig. 6(d) has been replotted in Fig. 7 as a function of wavelength. The data from Fig. 6(c) was converted to wavelength-space using the estimated convective velocity, $u_c = 0.8u_\infty = 860$ m/s.[30] As expected for a turbulent boundary layer, the scales present span the full range of wavelengths.

The time series for a single off-surface position and the overall signal root mean square (RMS) as a function of off-surface height for each of the three beam waists tested are shown in Fig. 8. The FLDI fluctuations generally follow the same pattern as the values from the DNS, but again at a lower amplitude. Increasing the beam waist results in decreasing the FLDI measurement amplitude. This trend agrees with prior studies on turbulent jets.[24,26] The same amplitude trend can be seen with the RMS fluctuations plot. Note that the spikes for the 3 μm beam waist (which has the largest profiles of the three waist sizes starting about 0.1 mm from the foci) near $y = 1$ mm and $y = 4$ mm, as well as the RMS increase in the simulated measurements right at the wall, correspond to edges in the DNS subfields and are likely nonphysical. The RMS fluctuation curves can roughly be shifted to go from one beam waist curve to another by scaling the values using the following equation:

$$\mathrm{rms}(\Delta\rho)_{new} \approx \mathrm{rms}(\Delta\rho)_{orig}\frac{w_{0,orig}}{w_{0,new}}. \tag{7}$$

This scaling leads to a beam waist of approximately 1.3 μm recovering the DNS density difference for this flow field.

Taking planar FLDI measurements along the beams was possible by saving the simulated FLDI measurements at each point on the optical (z) axis. These deconstructed measurements can more accurately be compared to the DNS density differences, found by subtracting the

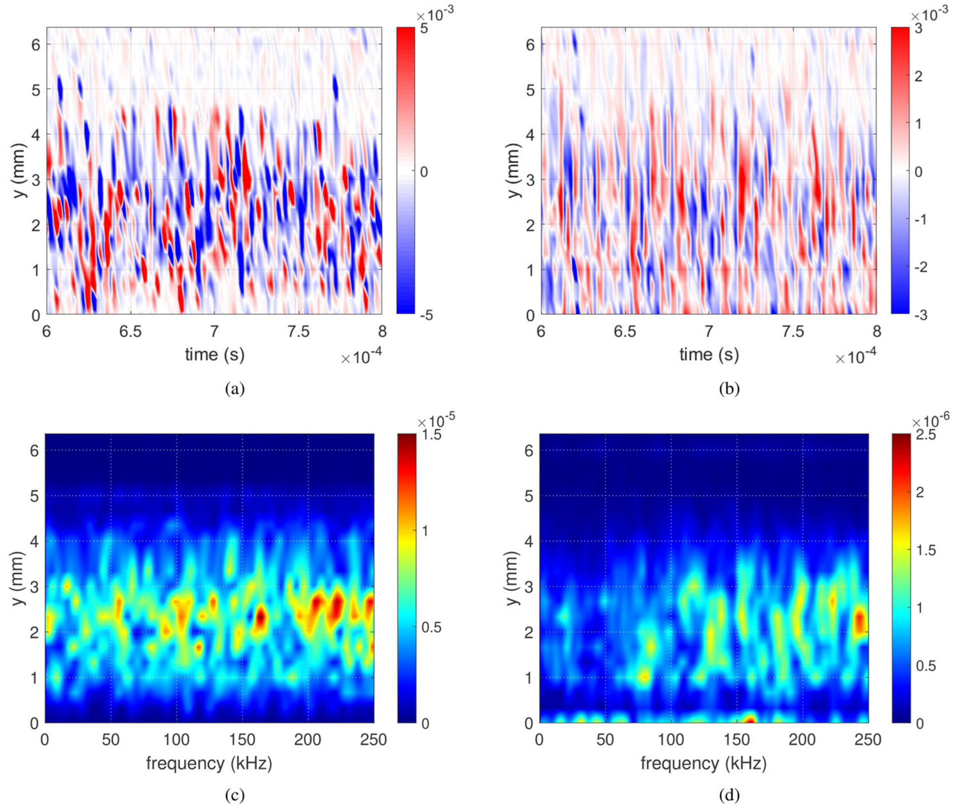

FIG. 6. Time series and power spectral densities for the DNS_{FS} $\Delta\rho$ values compared with the simulated FLDI $\Delta\rho$ values. Note the change in scale for the FLDI data: (a) DNS $\Delta\rho$ time series taken directly from DNS_{FS}, (b) simulated FLDI $\Delta\rho$ time series, (c) DNS $\Delta\rho$ PSD taken directly from DNS_{FS}, and (d) simulated FLDI $\Delta\rho$ PSD.

density values at the center of the two beams from each other at each position, since they do not incorporate the optical-axis integration that leads to ambiguity in the simulated measurement. This process was undertaken for each of the three beam waists computed, but is shown in detail for the 5 μm waist. There are two different ways to present these data: first, by observing the off-surface spatial fluctuations as a function of z for a single point in time, and second by studying the temporal fluctuations as a function of z for one off-surface position. These two views of the data are summarized in Figs. 9 and 10. In both views, $z = 0$ corresponds to the optical-axis location of the beam foci, and is also the point where the beams are closest to the cone surface for a given wall-normal position, y.

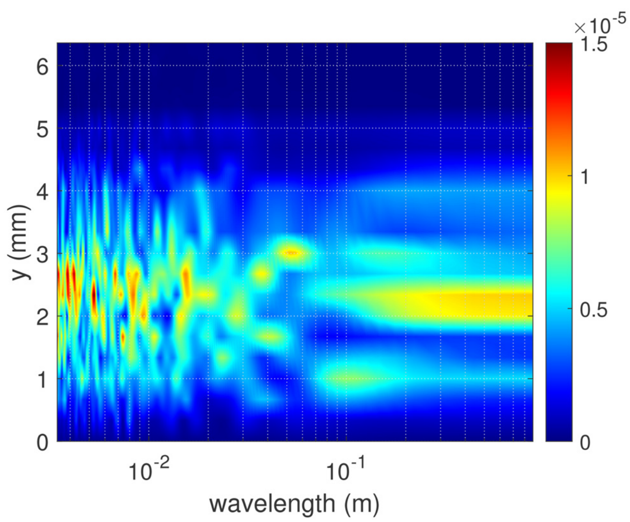

FIG. 7. DNS $\Delta\rho$ PSD taken as a function of signal wavelength.

In Fig. 9, results from the planar FLDI analysis are shown for off-surface fluctuations as a function of z for a single point in time. The DNS-derived density change values are shown in Fig. 9(a), while the simulated planar FLDI measurements are in Fig. 9(b). As expected, the FLDI planar density changes decrease in amplitude as the magnitude of z (i.e., the distance from the foci) increases. This trend is highlighted in Fig. 9(c), which plots the difference between the DNS and FLDI planar densities as a function of z; the differences between the DNS and FLDI increase with increasing z. Figure 9(d) plots the spatial RMS fluctuations in y as a function of z for each of the three beam waists. At $z = 0$ mm, the FLDI values nearly coincide with the DNS density change, while increasing magnitude of z results in overall lower FLDI amplitudes. Smaller beam waists correspond to greater signal suppression away from the region of interest due to the spatial averaging across the larger beam profiles away from the foci, as expected.[26]

As mentioned previously, the lower FLDI amplitudes as compared to the DNS-derived values is likely due to integration along the optical axis. This can be clearly observed in Fig. 9(b), which includes the spatial averaging that occurs across the beam profile, but deconstructs the FLDI measurement to show each value along the optical

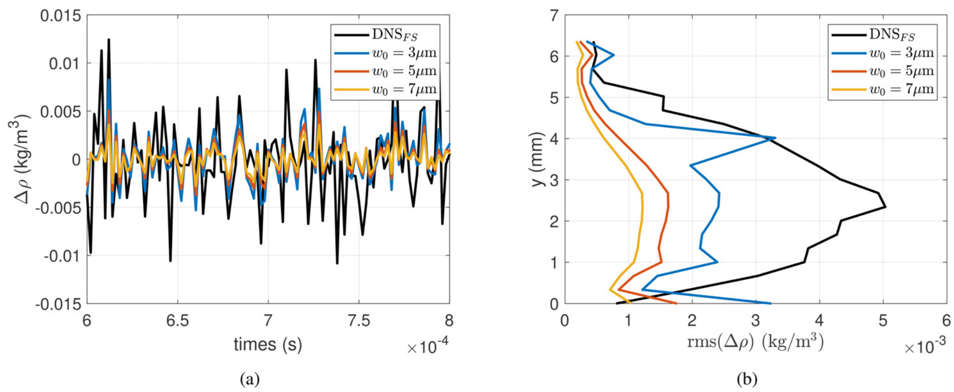

FIG. 8. Time series and RMS for each of the three beam waists tested: (a) time series at $y = 2.3432$ mm above the surface and (b) wall-normal RMS fluctuations.

axis (i.e., along the z direction). While the FLDI does somewhat suppress fluctuations away from $z = 0$ mm, there is still signal present in those regions that will be incorporated into the final FLDI measurement. By looking across a single height, y, it is easy to see both positive and negative density changes. These oppositely signed signals can cancel each other out, ultimately resulting in a lower FLDI amplitude than the true, point-measurement at $z = 0$ mm obtained directly from the DNS.

In Fig. 10, results from the planar FLDI analysis are displayed for temporal fluctuations as a function of z for a single position off-surface. Figure 10(a) displays the DNS-derived values while Fig. 10(b) shows the planar FLDI values for the $w_0 = 5$ mm case. As with the previous results, the FLDI results are similar to the DNS values, with the exception that their amplitudes decrease as z increases. Figure 10 (c) highlights this effect by plotting the difference between the DNS and FLDI values as functions of z and time. Higher percentages are desired for regions away from the foci to suppress signals outside the area of interest An ideal point-measurement would have a percent difference of 0% at $z = 0$ mm and of 100% at all other positions. The RMS fluctuations in time for each beam waist are plotted in Fig. 10(d). As before, smaller beam waists correspond to greater signal suppression as z increases (due to the larger beam profiles away from the foci). With this view, however, the width of the turbulent boundary layer through which the beams traverse is more apparent; the DNS signal is relatively constant between $z = -10$ and 10 mm.

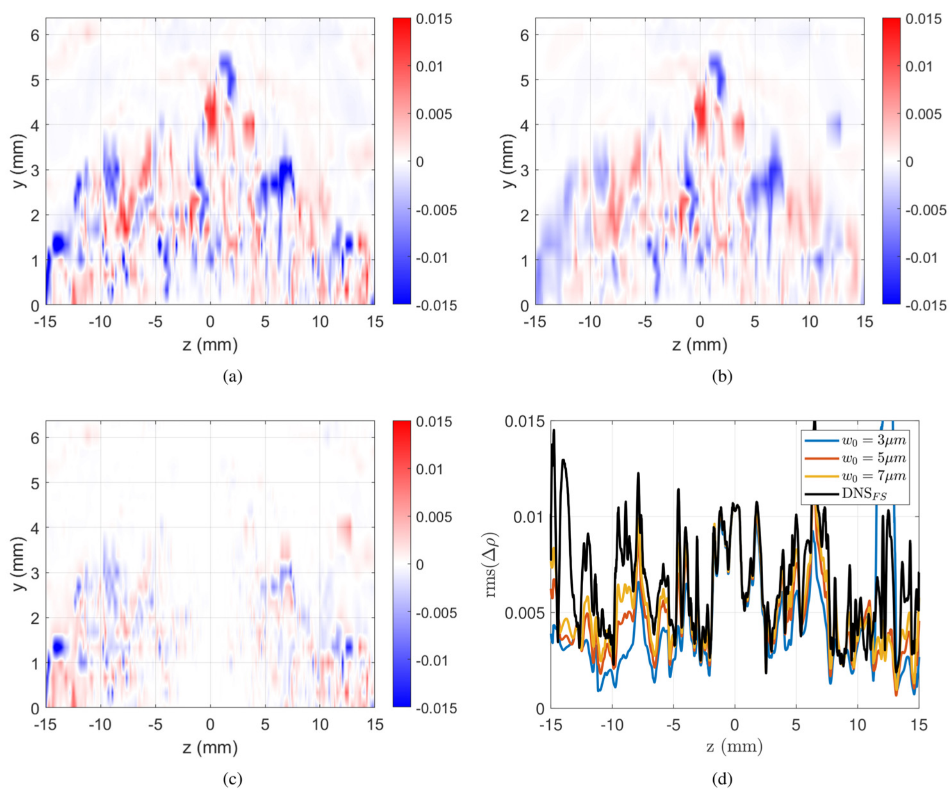

FIG. 9. Planar $\Delta\rho$ values as a function of spanwise position z at time 6.5×10^{-4} s from the (a) DNS$_{FS}$ and (b) simulated FLDI, (c) the difference between DNS and FLDI planar density change values, and (d) spatial RMS comparison.

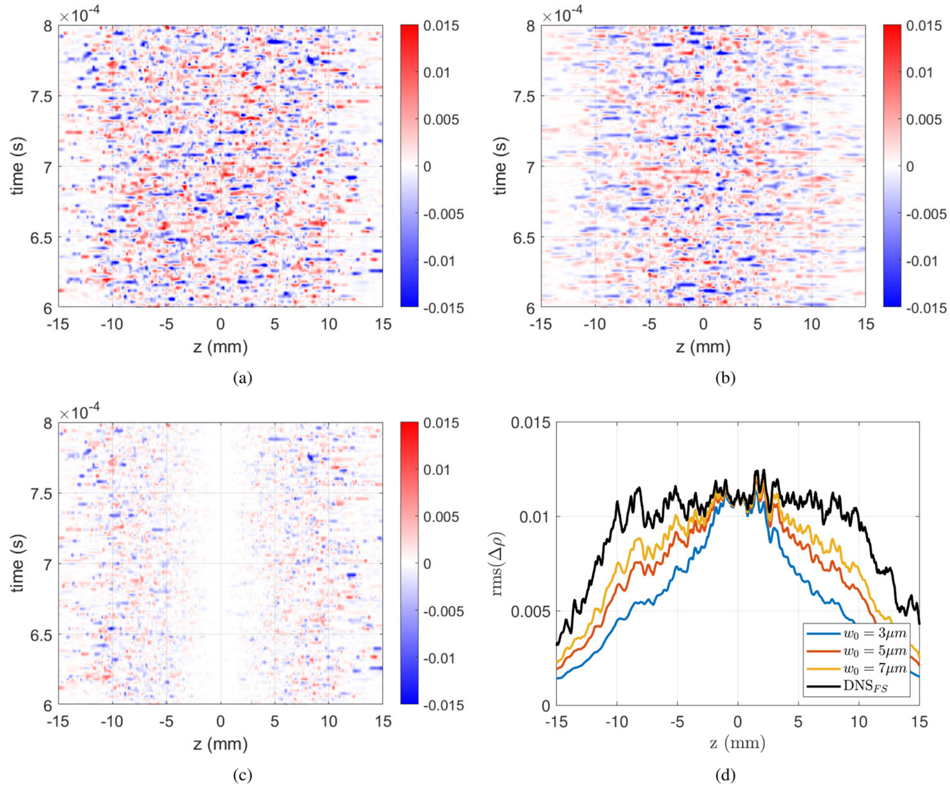

FIG. 10. Planar $\Delta\rho$ values as a function of spanwise position z at wall-normal position 2.3432 mm from the (a) DNS$_{FS}$ and (b) simulated FLDI, (c) the difference between DNS and FLDI planar density change values, and (d) temporal RMS comparison.

By plotting the percent difference between the DNS RMS and the planar FLDI RMS as a function of z (Fig. 11), it is possible to get an estimate for a scalar integration length L for each beam waist. In this case, a 5% cutoff was utilized, resulting in L values of 2.45, 3.68, and 5.35 mm for the 3, 5, and 7 μm beam waists, respectively. Using these constant results in overall simulated FLDI amplitudes more closely representative of the DNS values for this particular flow field. Interestingly, these estimated sensitivity lengths are similar in ratio to their corresponding beam waists. Note, however, that this similarity is just an observation and further investigation is necessary to determine if it holds for a general case.

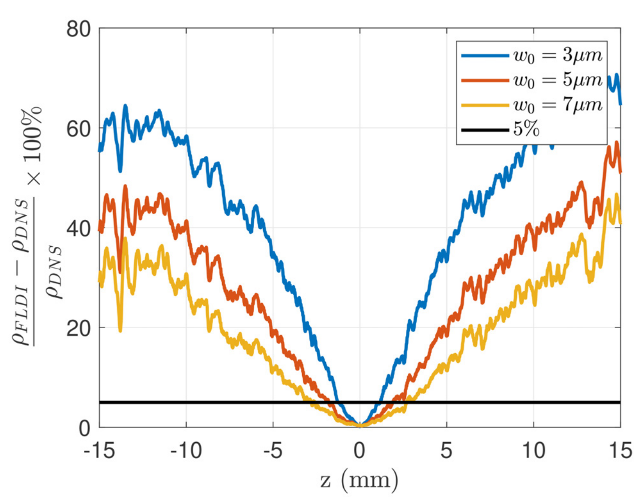

FIG. 11. Percent difference between DNS-derived density changes and planar FLDI density changes for the full-scale simulation.

In addition to the FLDI simulations run with the beam foci at $z = 0$ mm, several runs were made with the beams at $y = 2.3432$ mm and the foci at different z positions. This setup models an FLDI placed off-centerline in the turbulent boundary layer, and helps visualize how much the off-axis signal suppression provided by the FLDI is significant in a hypersonic turbulence experiment. Figure 12 displays the spanwise positions of the FLDI beam foci as red dots overlaid on a snapshot of the flow field for this spanwise-sensitivity study. Similar studies, both computational and experimental, have been conducted in

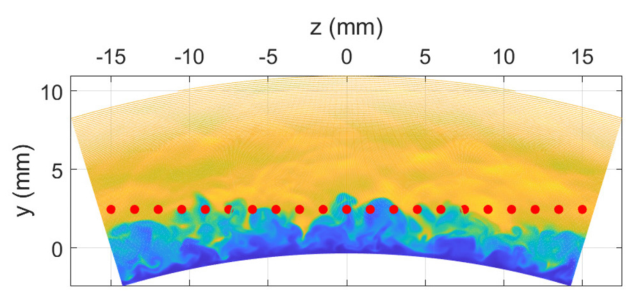

FIG. 12. Foci positions for the FLDI beams in the spanwise simulation.

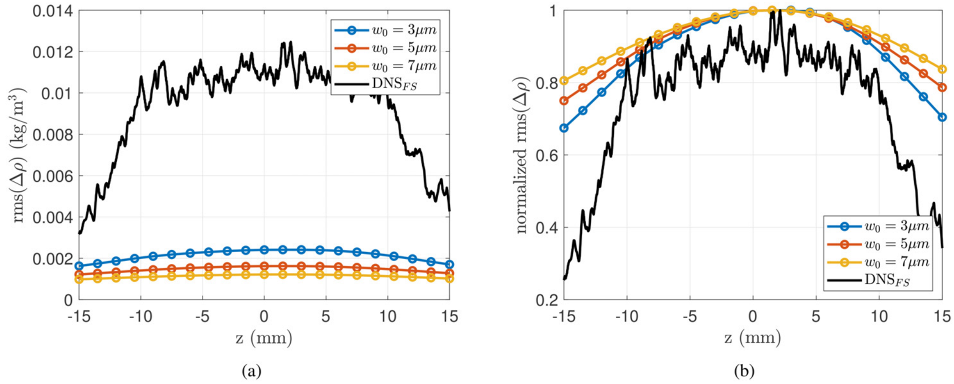

FIG. 13. RMS fluctuations of the simulated FLDI as a function of beam foci position along the optical (z) axis. The wall-normal position of the beams was $y = 2.3432$ mm for all cases: (a) dimensional RMS and (b) RMS normalized by maximum value.

the past using turbulent jets,[2–4,26] and were generally undertaken to help understand the sensitivity region of the FLDI.

Figure 13 plots the dimensional and normalized RMS falloff from the spanwise-sensitivity study using the full-scale DNS. The "true" density difference taken directly from the DNS as a function of z is plotted in black. This flow field differs from previously studied turbulent-jet FLDI simulations in that the turbulent boundary layer that the laser traverse is much thicker than the narrow-diameter jets usually used to probe the FLDI sensitivity region. Therefore, it should be expected that the signal falls off more slowly. Prior jet simulations on Gaussian beams have found that smaller beam waists (and, therefore, larger beam profiles away from the foci) resulted in faster sensitivity roll-offs, but also generally decreased the peak RMS as after a certain size.[26] With an axisymmetric turbulent boundary layer, however, this reversal in peak RMS was not observed. This is either due to the thicker region of turbulence traversed or was just not observed due to the limited number of beam waists tested.

2. Spatially averaged DNS

With the baseline FLDI results from the full-scale DNS characterized, the spatially averaged DNS was run through the FLDI simulation. The overall time series and associated PSDs are plotted in Fig. 14 for $w_0 = 5\,\mu$m. These results are similar to the full-scale FLDI results shown in Figs. 6(b) and 6(d), but have slightly lower amplitudes. Since the only difference in the FLDI simulation between this spatially averaged result and the full-scale one is the lack of small-scale flow structures, this amplitude difference is likely due to that change. The FLDI is most sensitive to small structures near the foci, where its largest signal is obtained. By filtering out these structures, the flow field has less fluctuations to measure in general, resulting in a lower FLDI signal overall. The spatially averaged DNS-derived time series and PSD similarly had lower amplitudes relative to the full-scale DNS-derived values.

For a more quantitative comparison between the full-scale and spatially averaged DNS and FLDI results, Fig. 15 plots time series and RMS plots for all four cases with $w_0 = 5$ mm. In Fig. 15(a), the time series for $y = 2.3432$ mm is shown. The DNS-derived density changes are similar, with the spatially averaged results generally having a slightly lower magnitude. Likewise, the FLDI results are nearly overlapping, again with the spatially averaged case having a slightly lower overall magnitude. In Fig. 15(b), the temporal density-difference RMS is plotted as a function of y for the four cases. Note that the increase in RMS at the wall is likely due to the beams clipping with the edge of the defined flowfield. The simulated results again show the spatially averaged cases having lower overall RMS as compared to the full-scale ones, for both the density differences derived directly from the DNS and those simulated from the FLDI. Interestingly, the change in RMS between the two FLDI results is actually much smaller than the difference between the DNS-derived values. This is likely due to the fact that the FLDI suppresses small-scale signals at much shorter distances from the foci than it does larger signals. In both FLDI cases, these

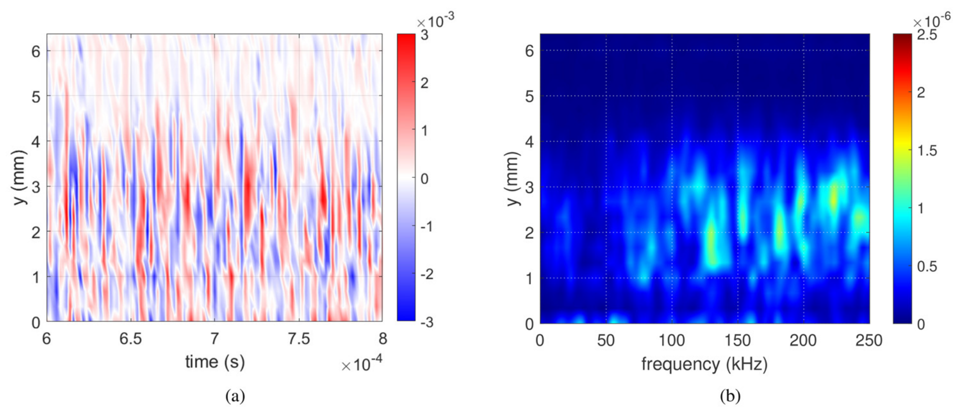

FIG. 14. Time series and power spectral densities for the simulated FLDI $\Delta\rho$ values, $w_0 = 5\,\mu$m: (a) simulated FLDI $\Delta\rho$ time series and (b) simulated FLDI $\Delta\rho$ PSD.

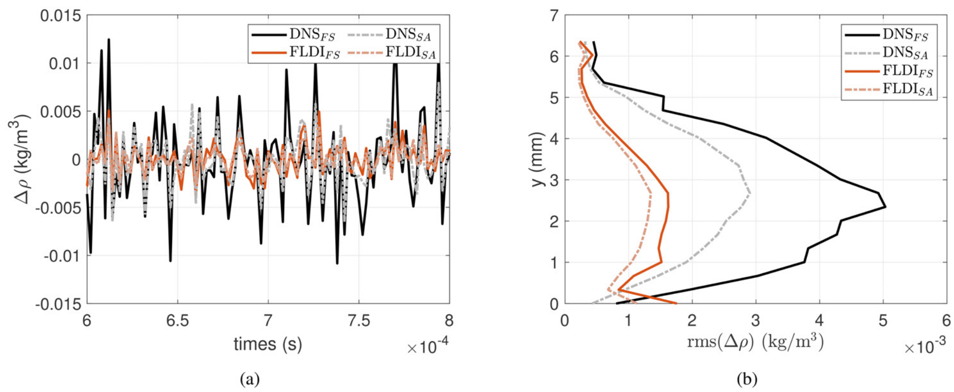

FIG. 15. Time series and RMS for the original and spatially averaged DNS with $w = 5\,\mu$m: (a) time series at $y = 2.3432$ mm above the surface and (b) wall-normal RMS fluctuations.

larger signals will still be integrated into the overall FLDI measurement. However, the smaller signals only present in the full-scale FLDI RMS are only incorporated into the signal for the z positions closest to the foci, making them an overall smaller part of the FLDI RMS as compared to the pure DNS RMS.

PSD line plots and ratios are displayed in Fig. 16 to help further analyze the impact of these small scales on the FLDI frequency response. In Fig. 16(a), the PSDs from the DNS-derived density change is shown with a black solid line for the full-scale results and a gray dashed line for the spatially averaged ones. Similarly, the FLDI simulation results are shown with a solid orange line for the full-scale output and a dashed lighter line for the spatially averaged output. As shown with the previous plots, the FLDI results have a lower amplitude than the DNS-derived ones, and also experience some suppression of the lower frequency signals not present in the DNS results. Figure 16(b) plots the ratios between the spatially averaged and full-scales results for the DNS-derived and FLDI simulation density differences. The DNS-derived results are relatively constant, with the spatially averaged values generally reaching between 20% and 40% of the full-scale amplitudes. For the FLDI simulation results, however, the spatially averaged magnitudes are between 60% and 80% for frequencies greater than 50 kHz, but drop down to 40%–60% for frequencies below that. This variation across frequency demonstrates a greater low-frequency signal suppression occurs when the small-scale structures are not present in the flow, as compared to the full-scale case.

Deconstructed planar FLDI measurements were compared to the DNS at a single height off-surface in Fig. 17. Figure 17(a) plots the temporal RMS as a function of z for all three beam waists as well as the spatially averaged DNS-derived values. A similar trend to the full-scale results from Fig. 10(d) is seen, with smaller beam waists (and, therefore, larger beam profiles away from the foci) corresponding to more signal suppression moving away from the region of interest. The percent difference between the FLDI and DNS values are plotted in Fig. 17(b). Using the same criteria as with the full-scale FLDI results (a 5% difference cutoff), scalar sensitivity lengths of $L = 4.18$, 6.25, and 10.34 mm were found for $w_0 = 3$, 5, and 7 μm, respectively. These values are nearly double those from the full-scale test, indicating that the off-axis signal is less suppressed for FLDI measurements with a flow field that excludes the smallest-scale structures.

Figure 18 encapsulates the spanwise-sensitivity results for the different flow field cases for each beam waist tested, obtained by running the FLDI simulation with the foci at different z positions (the same positions from Fig. 12 from the full-scale test). As with the full-scale DNS results shown previously, smaller beam waists (and larger beam profiles away from the foci) correspond to higher peak RMS measurements and faster signal falloff away from $z = 0$ mm for the spatially averaged cases. Comparing equivalent beam waists for the full-scale and spatially averaged DNS results in Fig. 18(a) reveals that removing the small-scale structures results degrades the FLDI measurements in both peak RMS values and spanwise signal falloff. This slower falloff is highlighted in the normalized results [Fig. 18(b)] and can explain differences between FLDI simulations made with LES flow fields and experimental measurements, such as with the narrow-diameter jet tests conducted by Benitez *et al.*[26]

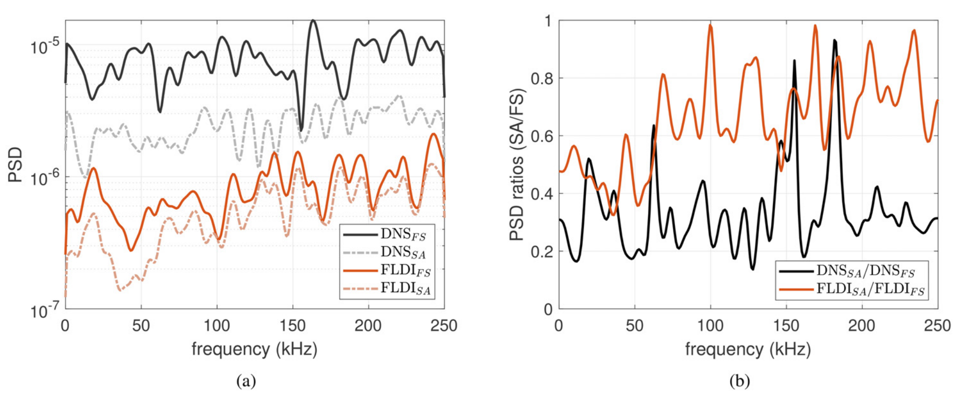

FIG. 16. PSD line plots and ratios for the original and spatially averaged DNS and FLDI simulations at $y = 2.3432$ mm above the surface with $w = 5\,\mu$m: (a) PSD line plots and (b) ratios between spatially averaged and full-scale PSDs.

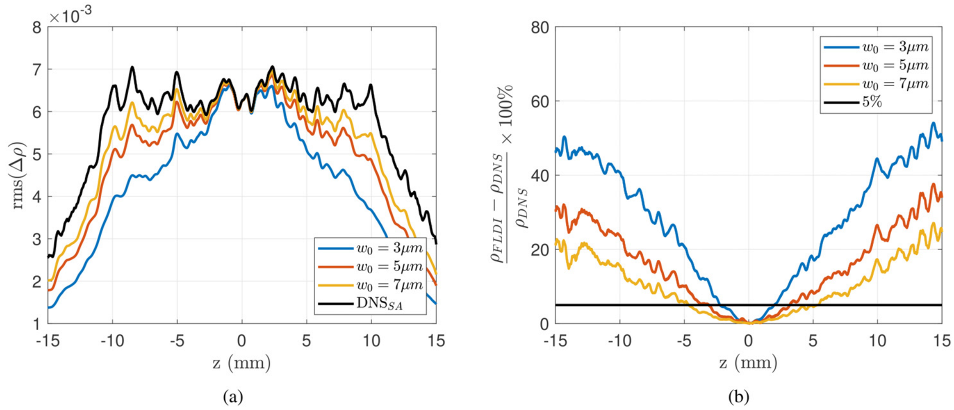

FIG. 17. Temporal RMS and percent difference between DNS-derived density changes and planar FLDI density changes at $y = 2.3432$ mm for the spatially averaged simulation: (a) temporal RMS comparison and (b) percent difference between DNS-derived density changes and planar FLDI density changes.

3. Low-frequency signal suppression

To better understand the cause of the low-frequency roll-off experienced by the FLDI results in both the full-scale and spatially averaged cases, FLDI transfer functions were computed and compared to the normalized simulation results. It has been well-documented that there are two key aspects of a physical FLDI that distinguish it from an idealized system: the finite separation between the two beams and the finite dimensions of the beam profiles.[5,23,24,26,27] These two features can be isolated to look at the affect of each independently when deriving a transfer function for an FLDI system. The definitions for the beam separation and profile size effects for a sinusoidal signal centered at the beam foci propagating in the x direction are given in the following equations, respectively:

$$H_{\Delta x} = \left| \sin\left(\frac{\pi \Delta x}{\lambda_s}\right) \right|, \tag{8}$$

$$H_w = \frac{w_0 \lambda_s \sqrt{2\pi}}{2L_z \lambda} \exp\left(-\frac{w_0^2 \pi^2}{2\lambda_s^2}\right) \operatorname{erf}\left(\frac{L_z \lambda \sqrt{2}}{2w_0 \lambda_s}\right). \tag{9}$$

Here, λ_s is the wavelength of the signal, while λ is the wavelength of the laser, in this case 633 nm. Additionally, L_z is the half-width (along the optical axis) of the sinusoidal signal. In order to use frequency space rather than wavelength space, the convective velocity of $u_c = 0.8u_\infty = 860$ m/s[30] was used to convert the signal wavelength to signal frequency ($f = u_c/\lambda_s$).

These equations have been derived by various methods in previously published literature.[5,23,27,36,37] Note, however, that there is a discrepancy between some definitions of $H_{\Delta x}$ between these sources, which will be discussed later.

Some FLDI sensitivity studies have gone further by introducing a transfer function for the flow field as well, such as when a narrow-diameter turbulent jet is probed.[24] However, from Figs. 10(d) and 17(a), this flow field appears to be relatively constant between $z = \pm 10$ mm. Therefore, for this case, only $H_{\Delta x}$ and H_w will be used, along with a signal half-width of $L_z = 10$ mm. Note however that in experimental tests of similar flows, high-intensity off-plane disturbances are common, such as turbulent shear layers. These off-centerline flows can have an impact on the FLDI measurements taken,[25] and would not be accounted for in this implementation of the transfer functions.

To capture the effects of both aspects of the nonideal FLDI, the two transfer functions can be multiplied, as in the following equation:

$$H = H_{\Delta x} H_w. \tag{10}$$

The contribution from each transfer function and the overall transfer function, H, are displayed in Fig. 19. Note that the horizontal axis extends far beyond the frequencies analyzed in this paper to allow for visualization of the amplitude drops at high frequency. From this plot, it can be seen that the finite spacing between the beams, the effect of which is captured by $H_{\Delta x}$, leads to both an exponential low-frequency roll-off as well as narrow-band signal drops at discrete frequencies.

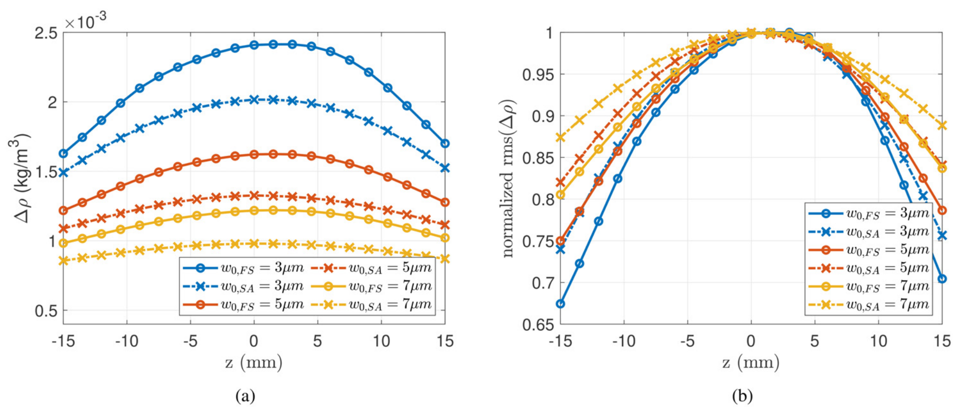

FIG. 18. RMS fluctuations with beam foci position for the original and spatially averaged DNS for all three beam waists: (a) dimensional RMS and (b) normalized RMS.

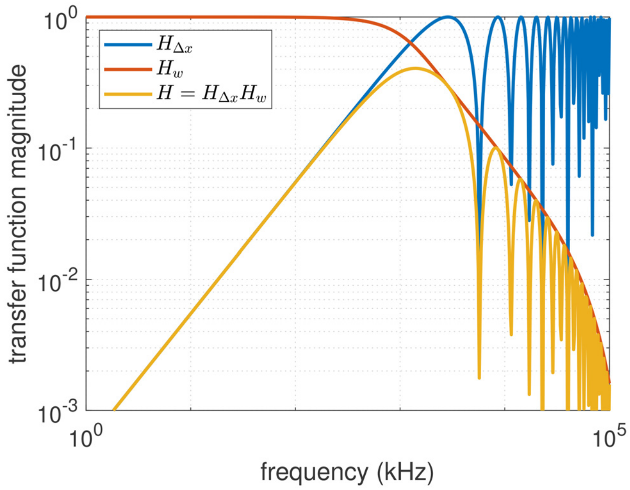

FIG. 19. FLDI transfer functions, $w_0 = 5\ \mu$m.

The wavelengths of these local minima are defined by Eq. (11), while the local maxima are defined with Eq. (12):

$$\arg\min_{\lambda_s} H_{\Delta x} = \left\{ \frac{\Delta x}{n} : n \in \mathbb{Z}^+ \right\}, \tag{11}$$

$$\arg\max_{\lambda_s} H_{\Delta x} = \left\{ \frac{2\Delta x}{2n-1} : n \in \mathbb{Z}^+ \right\}. \tag{12}$$

These outcomes are logical, when imagining two points along a sinusoidal curve, as is the case here given the sinusoidal signal assumption. The finite beam profile size, with effects capture by H_w, leads to a roll-off of the higher frequencies. This property essentially acts as a low-pass filter. By combining both effects, signal suppression can be seen at both lower and higher frequencies, along with signal drop-outs at sub-multiples of the beam spacing.

From this combined effect, it is apparent that H_w does not have a significant contribution to the FLDI signal for frequencies below around $f = 1000$ kHz (corresponding to signal wavelengths greater than 0.86 mm). This threshold is well above the frequency band of the DNS results. Therefore, only $H_{\Delta x}$ should dominate the simulated FLDI measurements. Additionally, since H_w only is significant for the smallest wavelengths, the overall PSD trend for the full-scale and spatially averaged FLDI simulations should similarly follow the $H_{\Delta x}$ curve. Note that this is only the case for a signal centered at the foci. If the signal is shifted along the optical axis such as it was in the spanwise-sensitivity studies, the H_w curve will shift to the left, reducing the low-pass filter cut-off frequency. Nevertheless, from this information it is apparent that the cause of the low-frequency signal suppression observed in the experiments is due to the finite-spacing of the FLDI beams.

Normalized PSD line plots for both the full-scale and spatially averaged FLDI results are displayed in Fig. 20, along with the computed transfer functions, H, for each of the three beam waists tested. As expected given the transfer function discussion above, little difference is seen in the trends for the full-scale and spatially averaged results. Both sets of FLDI simulations follow the same transfer function curves for frequencies greater than 40 kHz, with H capturing the low-frequency signal suppression previously observed.

Now that this low-frequency falloff has been linked to the finite beam spacing for the simulated FLDI, the discrepancy in the literature for the definition of $H_{\Delta x}$ can be addressed. Schmidt and Shepherd,[23] Fulghum,[37] and Hameed and Parziale[5] utilize a sinc() function for this term, while Lawson and Austin,[27] Ceruzzi *et al.*,[36] and this paper use a sin() function. This difference is not so much an error between sources as a difference in definitions. It stems from the former authors using the transfer function with definition $H = \frac{\max\left|\frac{\Delta\Phi}{\Delta x}\right|}{\frac{d\Phi}{dx}_{x=0}}$, which directly compares a realistic FLDI to an idealized system. The latter authors assume H is instead the FLDI phase change ($\Delta\Phi$) or density change ($\Delta\rho$) given a broadband signal of constant amplitude across all wavelengths. Lawson and Austin[28] show an equivalency between the two forms with the introduction of a $\frac{1}{2L_z}$ scaling factor through their Eqs. (19) and (20). Interestingly, the sinc() form of $H_{\Delta x}$ removes the low-frequency dependence of the transfer function, instead maintaining a magnitude of unity for all small-wavenumber signals.

B. DLR FLDI simulation results

The same DNS density fields were used as input to the DLR FLDI simulation as well. An initial simulation was conducted to compare the output of DLR FLDI code with that of the AFRL code. Once the codes were verified to produce equivalent results, the DLR FLDI model was used to study the FLDI instrument in a parametric analysis, by varying key characteristics of the system. The study was aimed at

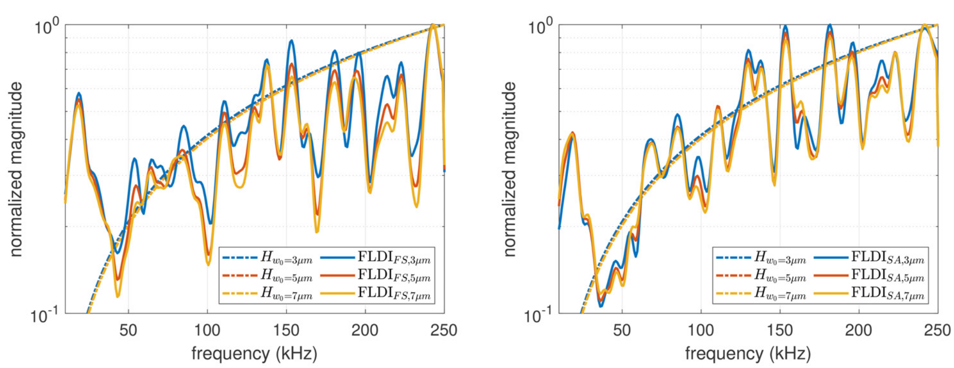

(a) (b)

FIG. 20. Normalized PSD line plots and transfer function for the full-scale and spatially averaged FLDI simulations at $y = 2.3432$ mm above the surface: (a) full-scale FLDI PSDs and (b) spatially averaged FLDI PSDs.

providing further insight on any possible differences between measurements obtained with the many FLDI configurations that can be found in the literature, when probing a hypersonic turbulent boundary layer.

1. Code-to-code comparison

Since the AFRL and DLR codes were independently implemented, it is important to verify that their outputs are equivalent. Even though the basic equations used in both codes are identical, the effects, if any, of the distinct approaches to data preprocessing and interpolation must be quantified before any comparative analysis can be made.

Figure 21 shows an example of time series of total phase shift ($\Delta\Phi$) obtained with the two models, for a randomly selected probing location. Minute localized differences can be observed across the time series, which are attributed to the different data interpolation methods. Nonetheless, the two time series correlate with 99.7%, confirming that the outputs of the two models are essentially the same. A qualitative comparison of the topology of density differences over time across multiple probing heights obtained with the two models (not shown) indicated this agreement with hold in a general manner.

2. Parametric analysis

The parametric analysis of the FLDI response presented here is motivated by the increasing variations of FLDI configurations already present in the literature, each having their own advantages and disadvantages. Four parameters are chosen for analysis: the divergence of the beams; the cross section intensity distribution of the beams; the cross section shape of the beams; and the direction of differentiation. For each case, only a single parameter is varied. All variations of configuration are implemented on a base standard configuration identical to the one used in the previous sections, in particular with beam waist $w_0 = 5\,\mu$m.

The divergence of the beams is akin to the beam waist variation already discussed in the previous sections. In this section, it is taken to

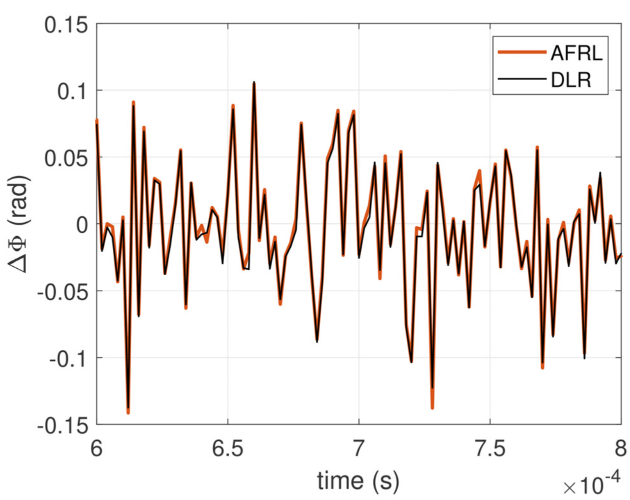

FIG. 21. Time series of total phase shift at $y = 2.38$ mm above surface and $w_0 = 5\,\mu$m, obtained with the AFRL and DLR FLDI models.

a limit where the beams have no divergence at all, presenting a constant radius of 5 μm. This situation would be equivalent to a basic laser differential interferometer (LDI), without the focusing aspect of FLDI. For the intensity distribution of the beams, a uniform intensity is applied. This is similar to having a top-hat beam profile, or using a stretched beam to illuminate multiple photodetectors, such as the multipoint line FLDI setup.[38] In the case of beam shape variation, an elliptical beam of arbitrary eccentricity of 0.85 stretched in the streamwise direction is adopted. This is to some extent representative of cylindrical FLDI setups.[20,39] Finally, an FLDI setup with wall-normal differentiation direction is evaluated. Although a streamwise differentiation direction is much more common in the literature, the analysis will show that there is benefit in considering both directions.

For each of the four cases, computational FLDI simulations were performed similarly to Sec. III A 1. The pointwise relative differences of $\Delta\rho$ PSDs for each case in comparison to the standard configuration [Fig. 6(d)] are shown in Fig. 22.

Figure 22(a) shows an overall larger $\Delta\rho$ PSD magnitude for the case with collimated 5 μm beams, in comparison to the setup with conventional focused beams. The effect looks more pronounced in the inner portion of the boundary layer and in the far field. This is, however, an artifact due to the representation of differences in relative terms, since the PSD magnitude in those regions is very small in the first place, as seen in Fig. 6(d). Notwithstanding, the overall larger magnitude follows the trend already highlighted previously, that the FLDI measurement amplitude increases with smaller beam sizes. Furthermore, the fact that this effect is observed across the entire frequency range with little to no frequency dependence agrees with the observation in Sec. III A 3 that the effect of beam profile size (H_w) is negligible for this case.

The comparisons for uniform beam intensity and elliptical cross section shown in Figs. 22(b) and 22(c), respectively, show a damped signal across the spectrum. This effect is similar to as if the beam waist of the FLDI setup was larger, and is more pronounced for the case of uniform beam intensity. This represents a degraded performance in comparison to a beam of Gaussian distribution using the same optics. However, once again, no distinct trends can be seen across the spectrum. This means that the measured density disturbances should not be expected to be affected by these design choices, as long as the lower amplitudes are properly taken into account when postprocessing the data.

Finally, the wall-normal differentiation comparison shown in Fig. 22(d) highlights some interesting characteristics in the context of hypersonic turbulent boundary layer investigation. First, the large positive relative difference in many regions indicate that the vertical differentiation may be more sensitive, although this is exacerbated by the low PSD magnitudes in those regions, as above-mentioned. Furthermore, starting at 100–200 Hz, depending on the off-surface height, the measured magnitudes of $\Delta\rho$ PSDs become quite similar. This independence of differentiation direction is an indication of isotropy of the density fluctuations. Therefore, the comparison between measurements using distinct differentiation distances may present a means to experimentally measure the scale of turbulence isotropy, in terms of density fluctuations.

IV. CONCLUSION

Hypersonic turbulence is a challenging flow regime to study due to the large scale of flow structure sizes present to be resolved. In

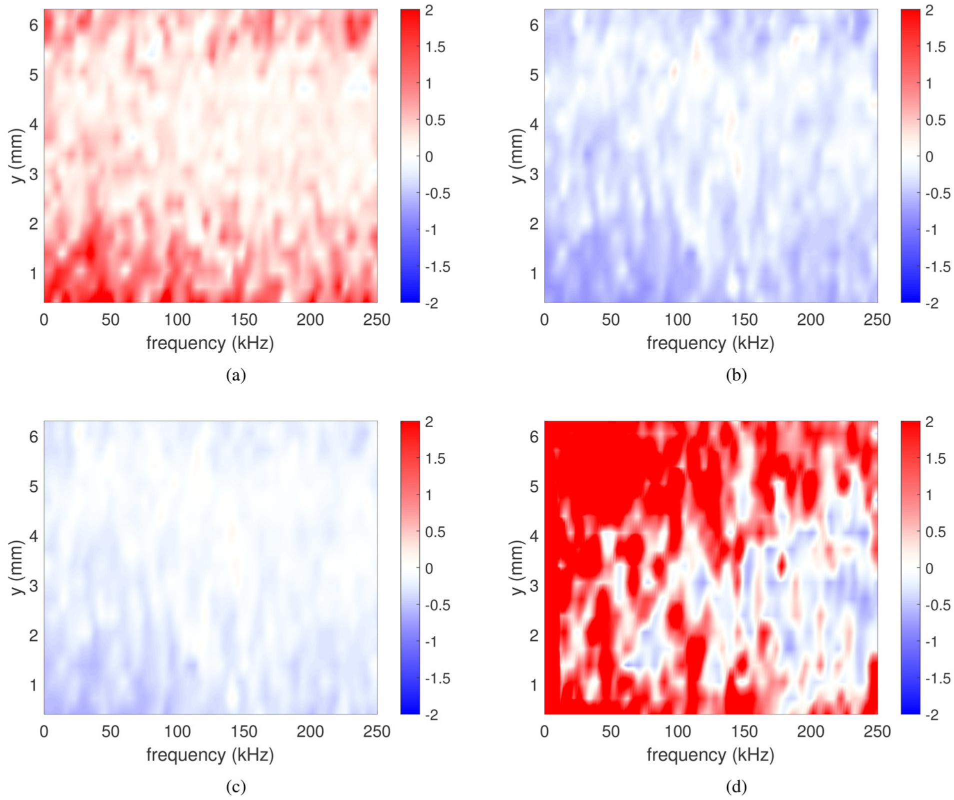

FIG. 22. Distributions of pointwise relative differences of PSDs of $\Delta\rho$, between FLDI setups with different parameter variations and the standard FLDI configuration shown in Fig. 6(d): (a) collimated beams, (b) uniform beam intensity, (c) elliptical cross section, and (d) wall-normal differentiation.

experiments, FLDI has become a common diagnostic for this regime, and has been the focus of several computational studies to understand the utility and limits of the technique. While some studies have utilized DNS flow fields, others have used computationally cheaper LES models, which exclude the smallest scales from the flow. Consequently, some variations between experimental and computational FLDI measurements have been observed, that may be due to the lack of these structures in the simulation input.

To better understand the performance of FLDI in hypersonic turbulence and to determine the significance of these smaller flow structures, an FLDI simulation was run on two sets of flow fields derived from the same configuration. First, a full-scale DNS of a sharp cone at Mach 8 was run through the simulation to study how an FLDI responds to a hypersonic turbulent boundary layer. Then, a spatially averaged version of the DNS that filtered out the smallest-scale structures was run through the FLDI simulation to see its response to the same flow field excluding those smaller disturbances. Finally, a parametric analysis was conducted with variation of the FLDI setup parameters representative of the multiple types of FLDI already present in the literature.

Key outcomes of the research include the following:

- Simulated FLDI measurements result in lower-amplitude density changes than the true point values, likely due to integration along the optical axis.
- These measurements also resulted in a low-frequency roll-off of amplitudes that was determined to be due to the finite spacing between the two beams.
- Smaller Gaussian beam waists corresponded to greater suppression away from the foci.
- Less suppression away from the foci was observed for the spatially averaged case (which removed the smallest-scale structures from the flow) than for the full-scale case.
- A difference in definitions of a transfer function have led to a discrepency in the low-wavenumber behavior on an analytical FLDI in the literature.
- The parametric study showed that beams with elliptical shape or uniform intensity distribution yield overall lower measurement magnitudes in comparison to Gaussian and circular.
- The comparison between FLDI results using distinct differentiation directions highlighted frequency bands and locations within the boundary layer where the measured magnitudes of density perturbations are independent of the differentiation direction; this kind of comparison may, hence, provide an experimental method to measure the scale of turbulence isotropy.

Future work includes using a dispersion velocity[24] to define the convection velocity for the boundary layer. This removes the constant-convection-velocity assumption and replaces it with a velocity that is a function of signal frequency. Another potential investigation involves looking at the effect of integration length on the quantification of the FLDI using these simulation results. A high-fidelity DNS of a single second-mode wave will also be analyzed to better understand the FLDI response to this commonly measured signal.

ACKNOWLEDGMENTS

Computational resources were provided by the Department of Defense (DoD) High Performance Computing Modernization Program (HPCMP). Authors M. Aultman and L. Duan were supported by ONR grant N00014-23-1-2304 (Eric Marineau, Program Manager). Author J. Jewell was supported by ONR grant N00014-21-1-2603 (Eric Marineau, Program Manager). The authors thank Bryan Schmidt for sharing his initial FLDI simulation code and Ahsan Hameed for his excellent suggestions for the FLDI analysis.

AUTHOR DECLARATIONS

Conflict of Interest

The authors have no conflicts to disclose.

Author Contributions

Elizabeth Benitez: Conceptualization (lead); Formal analysis (lead); Investigation (lead); Methodology (lead); Validation (lead); Visualization (lead); Writing – original draft (lead); Writing – review & editing (equal). **Matthew Aultman:** Data curation (lead); Methodology (supporting). **Lian Duan:** Data curation (supporting); Supervision (supporting). **Giannino Ponchio Camillo:** Formal analysis (supporting); Investigation (supporting); Methodology (supporting); Validation (supporting); Visualization (supporting); Writing – original draft (supporting); Writing – review & editing (supporting). **Joseph Stephen Jewell:** Validation (supporting); Writing – review & editing (supporting).

DATA AVAILABILITY

The data that support the findings of this study are available from the corresponding author upon reasonable request.

REFERENCES

[1]G. Smeets and A. George, "Laser-differential interferometer applications in gas dynamics," Tech. Rep. R136/75, translated by A. Goetz, DTIC Citation ADA307458 (Institut Saint-Louis, 1975).
[2]A. Ceruzzi and C. Cadou, "Turbulent air jet investigation using focused laser differential interferometry," in *53rd AIAA/SAE/ASEE Joint Propulsion Conference*, Paper 2017-4834 (AIAA, Atlanta, GA, 2017).
[3]J. Lawson, M. Neet, I. Grossman, and J. Austin, "Static and dynamic characterization of a focused laser differential interferometer," Exp. Fluids **61**, 187 (2020).
[4]E. Benitez, J. Jewell, and S. Schneider, "Focused laser differential interferometry with contoured tunnel windows," AIAA J. **59**, 419–429 (2021).
[5]A. Hameed and N. Parziale, "Focused laser differential interferometric investigation of turbulent jet spectra," J. Spacecr. Rockets **59**, 1565 (2022).
[6]N. Parziale, J. Shepherd, and H. Hornung, "Reflected shock tunnel noise measurement by focused differential interferometry," in *42nd AIAA Fluid Dynamics Conference and Exhibit*, Paper 2012-3261 (AIAA, New Orleans, LA, 2012).
[7]J. Lawson and J. Austin, "Focused laser differential interferometer response to shock waves," Meas. Sci. Technol. **32**, 055203 (2021).
[8]G. Camillo and A. Wagner, "Focused laser differential interferometry post-processing methodology for flowfields with circular symmetry," Rev. Sci. Instrum. **94**, 045102 (2023).
[9]N. Parziale, J. Shepherd, and H. Hornung, "Free-stream density perturbations in a reflected-shock tunnel," Exp. Fluids **55**, 1665 (2014).
[10]J. Lawson and J. Austin, "Expansion tube freestream disturbance measurements using a focused laser differential interferometer," in *AIAA SciTech 2020 Forum*, Paper 2020-1064 (AIAA, Orlando, FL, 2020).
[11]G. Gillespie, A. Ceruzzi, and G. Laurence, "A multi-point focused laser differential interferometer for characterizing freestream disturbances in hypersonic wind tunnels," Exp. Fluids **63**, 180 (2022).
[12]N. Parziale, J. Shepherd, and H. Hornung, "Observations of hypervelocity boundary-layer instability," J. Fluid Mech. **781**, 87–112 (2015).
[13]A. Ceruzzi, B. Callis, D. Weber, and C. Cadou, "Application of focused laser differential interferometry (FLDI) in a supersonic boundary layer," in *AIAA SciTech 2020 Forum*, Paper 2020-1973 (AIAA, Orlando, FL, 2020).
[14]E. Benitez, J. Jewell, S. Schneider, and S. Esquieu, "Instability measurements on an axisymmetric separation bubble at Mach 6," in *AIAA Aviation 2020 Forum*, Paper 2020–3072 (AIAA, Virtual, 2020).
[15]F. Siddiqui, M. Gragston, and R. Bowersox, "Measurement of wall-cooling effects on hypersonic boundary- layer transition using focused laser differential interferometry," AIAA J. **60**, 6214 (2022).
[16]G. Camillo, A. Wagner, T. Toki, and C. Scalo, "Combined experimental and numerical investigation of a hypersonic turbulent boundary layer by means of FLDI and large-eddy simulations," Aerospace **10**, 570 (2023).
[17]E. Benitez, M. Borg, P. Paredes, S. Schneider, and J. Jewell, "Measurements of an axisymmetric hypersonic shear-layer instability in quiet flow," Phys. Rev. Fluids **8**, 083903 (2023).
[18]E. Benitez, M. Borg, S. Dungan, C. Brehm, and J. Jewell, "Focused laser differential interferometry performance over an axisymmetric model," in *AIAA SciTech 2024 Forum*, Paper 2024–1931 (AIAA, Orlando, FL, 2024).
[19]J. Jewell, N. Parziale, K. Lam, B. Hagen, and R. Kimmel, "Disturbance and phase speed measurements for shock tubes and hypersonic boundary-layer instability," in *32nd AIAA Aerodynamic Measurement Technology and Ground Testing Conference*, Paper 2016–3112 (AIAA, Washington, DC, 2016).
[20]A. Houpt and S. Leonov, "Focused laser differential interferometer for supersonic boundary layer measurements on flat plate geometries," in *2018 Plasmadynamics and Lasers Conference*, Paper 2018–3434 (AIAA, Atlanta, GA, 2018).
[21]M. Gragston, T. Price, K. Davenport, J. Schmisseur, and Z. Zhang, "An m-by-n FLDI array for single-shot, multipoint disturbance measurements in high-speed flows," in *AIAA SciTech 2021 Forum*, Paper 2021–0599 (AIAA, Virtual, 2021).
[22]J. Chism, M. Gragston, S. Peltier, and T. McManus, "Camera-based detection of FLDI for measurements in high-speed turbulent boundary layers," in *AIAA Aviation 2022 Forum*, Paper 2022–3474 (AIAA, Chicago, IL, 2022).
[23]B. Schmidt and J. Shepherd, "Analysis of focused laser differential interferometry," Appl. Opt. **54**, 8459–8472 (2015).
[24]A. Ceruzzi and C. Cadou, "Interpreting single-point and two-point focused laser differential interferometry in a turbulent jet," Exp. Fluids **63**, 112 (2022).
[25]E. Benitez, M. Borg, J. Hill, M. Aultman, L. Duan, C. Running, and J. Jewell, "Quantitative focused laser differential interferometry with hypersonic turbulent boundary layers," Appl. Opt. **61**, 9203–9216 (2022).
[26]E. Benitez, M. Borg, C. Rhodes, and J. Jewell, "Optical-axis spatial sensitivity of a simulated focused laser differential interferometer," AIAA J. **61**, 1925–1938 (2023).
[27]J. Lawson and J. Austin, "Recovering density disturbance spectra from FLDI. Part 1," Appl. Opt. **62**, 3042–3053 (2023).
[28]J. Lawson and J. Austin, "Recovering density disturbance spectra from FLDI. Part 2: Comparisons with previous methods," Appl. Opt. **62**, 3054–3061 (2023).
[29]K. Casper, S. Beresh, J. Henfling, R. Spillers, and B. Pruett, "Hypersonic wind-tunnel measurements of boundary-layer transition on a slender cone," AIAA J. **54**, 1250–1263 (2016).
[30]J. Huang, L. Duan, K. Casper, R. Wagnild, and N. Bitter, "Transducer resolution effect on pressure fluctuations beneath hypersonic turbulent boundary layers," AIAA J. **62**, 882–895 (2024).
[31]G. Jiang and C. Shu, "Efficient implementation of weight ENO schemes," J. Compute. Phys. **126**, 202–228 (1996).
[32]J. Williamson, "Low-storage Runge-Kutta schemes," J. Compute. Phys. **35**, 48–56 (1980).

[33]M. Martin, U. Piomelli, and G. Candler, "Subgrid-scale models for compressible large-eddy simulations," Theor. Comput. Fluid Dyn. **13**, 361–376 (2000).
[34]J. Gladstone and T. Dale, "Researches on the refraction, dispersion, and sensitiveness of liquids," Proc. R. Soc. London **12**, 317–343 (1863).
[35]N. Parziale, "Slender-body hypervelocity boundary-layer instability," Ph.D. thesis (California Institute of Technology, Pasadena, California, 2013).
[36]A. Ceruzzi, C. Neisess, B. McManamen, and C. Cadou, "Investigation of focused laser differential interferometry (FLDI) sensitivity function," in *AIAA SciTech 2021 Forum*, Paper 2021–1299 (AIAA, Virtual, 2021).
[37]M. Fulghum, "Turbulence measurements in high-speed wind tunnels using focusing laser differential interferometry," Ph.D. thesis (The Pennsylvania State University, State College, Pennsylvania, 2014).
[38]J. M. Weisberger, B. F. Bathel, G. C. Herring, G. M. Buck, S. B. Jones, and A. A. Cavone, "Multi-point line focused laser differential interferometer for high-speed flow fluctuation measurements," Appl. Opt. **59**, 11180 (2020).
[39]K. J. Hopkins, H. Porat, T. J. McIntyre, V. Wheatley, and A. Veeraragavan, "Measurements and analysis of hypersonic tripped boundary layer turbulence," Exp. Fluids **62**, 164 (2021).